



High detectivity and linear dynamic range in green light perovskite quantum dot photodetectors via surface passivation

Wei-Kuan Hung ^a, Kasimayan Uma ^{a,b}, Shu-Meng Yang ^{a,b}, Lung-Chien Chen ^a, Yu-Cheng Lin ^c,
Zong-Liang Tseng ^{b,*}

^a Department of Electro-Optical Engineering, National Taipei University of Technology, Taipei, Taiwan

^b Organic Electronics Research Center, Ming Chi University of Technology, New Taipei City, Taiwan

^c Department of electronics engineering, Ming Chuan University, Taoyuan City, Taiwan

ARTICLE INFO

Keywords:

Photodetector
Green emitting light
Ligand structure
Quantum confinement effect
Surface passivation

ABSTRACT

Perovskite quantum dots photodetectors (QPDs) are acclaimed for their exceptional sensitivity and responsivity across a wide spectral range. The low-cost fabrication of QPDs enables the development of multifunctional, high-performance optoelectronic devices with fewer defects, enhanced carrier mobility, and improved stability, leading to superior conversion efficiency. However, green-light-emitting FAPbBr₃ perovskites, in particular, remain relatively underexplored in the literature. In this study, we focused on synthesis of FAPbBr₃ green-light QPDs, utilizing didodecyldimethylammonium bromide (DDAB) ligands for the surface passivation. The DDA⁺ ion exhibits a stronger affinity for the negatively charged Br⁻ sites, and its shorter chain enhances effective surface passivation of the QDs, while also facilitating the transfer of photoexcited charges within the FAPbBr₃ QDs. The device (ITO/PCBM/FAPbBr₃-DDAB/TAPC/MoO₃/Ag) incorporating [6 % at 530 nm and a detectivity of 7.93×10^{12} Jones. Further, the performance of the FAPbBr₃ photodetector was significantly enhanced, leading to an increase in a Detectivity (D*) to 7.93×10^{12} Jones, a linear dynamic range (LDR) of 103.33 dB and on/off response time of 3.64 μs and 1.97 μs, respectively.

1. Introduction

Photodetectors (PDs) are a promising class of light-sensitive devices with the potential to revolutionize various fields, including optical communication [1–3]. This can be categorized into broadband and narrowband wavelength ranges based on the detectivity and absorption characteristics of the photoactive semiconductor materials used [4–7]. These semiconductors have the potential to drive advancements in photodetector technology, with applications in imaging and biomedical sensing [8–10]. PDs with hybrid structures have been investigated to enhance performance in ultraviolet or infrared light detection. In this research, a novel hybrid structure was introduced, combining zinc oxide (ZnO) nanorods with graphene quantum dots (GQDs) or carbon quantum dots (CQDs) to achieve improved detection capabilities [11]. This device achieved a photoresponsivity of 6.92×10^4 A/W and a detectivity of 1.78×10^{15} Jones under 365 nm light at a low bias of 2 V. Another study focused on using methylammonium lead iodide (MAPbI₃) perovskite film in conjunction with GQDs [12]. The addition of GQDs

improved light absorption, enhanced charge carrier generation, and promoted charge transport by forming a junction with the MAPbI₃ film. This resulted in a high-quality perovskite film with the PDs achieved a maximum detectivity of 6.5×10^{11} Jones and a responsivity of 12 A/W under a bias voltage of -3 V, which is three times higher than that of the pristine MAPbI₃ device.

Organic-inorganic halide perovskites have undergone significant development and garnered widespread attention in various fields [13, 14]. These materials are rapidly gaining popularity in scientific research due to their high light absorption efficiency, high carrier mobility, tunable energy gap, and low cost [8, 15, 16]. Perovskite quantum dots (PQDs) are nanoscale materials where electrons are confined within quantum dimensions, leading to unique properties that distinguish them from traditional semiconductors [17–21]. In PQDs, the confinement of electrons and holes causes the energy levels to become quantized, as the size of the quantum dot approaches the material's wavelength and is smaller than twice the Bohr radius [8, 22]. This quantization allows the band gap of the material to be adjusted by altering the size of the

* Corresponding author.

E-mail address: zlteng@mail.mcut.edu.tw (Z.-L. Tseng).

quantum dots, enabling precise tuning of their luminescence color. As the crystal size of perovskite materials are small, the energy levels of the electrons increase, leading to a widening of the bandgap. This increase in the HOMO-LUMO gap results in a shift of the emission wavelength toward shorter wavelengths. In Br-based perovskites, this effect causes the emission color to transition from green to violet, passing through blue as the particle size decreases [23–25]. Similarly, in I-based perovskites, the emission color shifts from near-infrared (IR) to green, progressing through red, orange, and yellow as quantum confinement increases. Due to these characteristics, PQDs have become essential materials in a wide range of optoelectronic applications, including light sensors, light-emitting diodes (LEDs), solar cells, biomedical detection, lasers, and other advanced technologies [26–32].

Recent studies have demonstrated PDs devices focus on green light wavelength selectivity using perovskite-based materials to achieve high efficiency [26,27,33]. One of the key advantages of green emitting perovskites is their ability to facilitate exciton diffusion to the interface between the donor and acceptor layers, where excitons quickly dissociate [34–36]. The significant efforts have been made to achieve green light emission using inorganic CsPbBr_3 perovskite, which is typically capped with long alkyl ligands and synthesized via the hot-injection method [16,31–34]. A large number of ligands are typically required for adequate surface passivation. Long-chain ligand pairs, such as oleic acid (OA) and oleylamine (OAm), are commonly used to cap the QDs surface by coordinating with unbound surface ions, resulting in mono-dispersed QDs [37,38]. However, these ligands can destabilize the QD surface, introducing defects that negatively impact the performance of LEDs and PDs [35,36,39]. This destabilization leads to reduced photoluminescence quantum yields, increased nonradiative recombination, and accelerated device degradation [40–42].

To mitigate these issues, single-ligand passivation strategies have been developed, employing halide ions and decylbenzene to effectively passivate Pb^{2+} ions with minimal impact on A-site vacancies [43–45]. However, A-site and X-site vacancies on the QD surface can still cause adverse effects, such as disrupting acid-base equilibria. Zwitterionic ligands, such as 3-(N,N-dimethyloctadecylammonio)-propanesulfonate and N-hexadecylphosphocholine, which contain both acidic and quaternary ammonium groups, have demonstrated potential in efficiently passivating surface defects [46,47]. This efficiency is primarily due to the quaternary ammonium groups' ability to prevent mutual or external acid-base neutralization. The introduction of shorter ligands has led to small modifications in PQDs, resulting in advanced methods to enhance their luminescent performance. For example, Dongdong et al. reported that replacing the long OA ligand with the shorter 2-hexyldecanoic acid (DA) ligand improved both stability and optical properties [48]. In another study, high-performance PQDs were synthesized using the shorter DA ligand in place of OA, achieving a high photoluminescence quantum yield (PLQY) of 96 % [48]. These QDs were used as green phosphors in high-performance light-emitting devices, exhibiting a luminous efficiency of 43.6 1 m/W with CIE coordinates of (0.2086, 0.7635) under a 15.3 mA driving current. Donglin Jia's research demonstrated that using 2-pentanol (2-PeOH) as a solvent to mediate ligand exchange can effectively remove the pristine insulating OAm ligands from the PQD surface, thereby reducing halogen vacancy defects [49]. Additionally, studies by Jinfei et al. and Hua et al. showed that shorter ligands, such as DDAB, can replace OAm and OA ligands, leading to fewer surface states, higher PLQY, and enhanced stability of the perovskite QDs [50–52].

When formamidinium iodide (FAI) in ethyl acetate (EtOAc) is used for synthesis of PQDs, the conductive short FA⁺ cations can effectively replace the OAm ligands, significantly enhancing charge carrier mobility within the PQDs solid films [53,54]. However, intense FAI ligand exchange can also lead to FA⁺ cations penetrating the perovskite lattice, forming $\text{FA}_{1-x}\text{Cs}_x\text{PbI}_3$ PQDs. Additionally, replacing the hydrophobic OAm ligands with hydrophilic FA⁺ ligands increases the susceptibility to moisture penetration, which can reduce the phase stability

of PQD devices [44,53,54]. Various fabrication methods, including solution processing and evaporation, have made perovskites both flexible and economical for manufacturing for perovskite photodetector [37,55,56]. However, perovskite PDs still face challenges related to stability, durability, and environmental impact. Therefore, exploring the characteristics, preparation methods, and application prospects of QPDs, along with proposing potential solutions and research directions, is essential at this time.

In this study, we demonstrate the fabrication of PDs using FAPbBr₃ green-light-emitting QDs, with surface passivation achieved through DDAB ligands. The DDAB ligands effectively displace dynamically bonded OA/OAm ligands and significantly reduce surface defects in the FAPbBr₃ QDs, leading to enhanced crystallinity and improved photoluminescence performance. The green-emitting FAPbBr₃ QDs exhibit a cubic structure, with surface ligands boosting carrier transport. The double-tailed cationic DDAB ligands, due to their hydrophobic nature, enable efficient ligand exchange while maintaining the structural integrity of the FAPbBr₃ QDs. By varying molar concentrations, we optimized ligand exchange efficiency, achieving a longer carrier lifetime at 0.2 mmol DDAB compared to 0.3 mmol. The device (ITO/PCBM/FAPbBr₃-DDAB/TAPC/MoO₃/Ag) fabricated with 0.2 mmol DDAB attained an EQE of 26.94 % at 530 nm and a D* of 7.93×10^{12} Jones. Additionally, the shorter ligand exchange process resulted in a LDR of 103.33 dB, with on/off response times of 3.64 μ s and 1.97 μ s, respectively.

2. Experimental method

2.1. Synthesis of the FAPbBr₃ QDs by the hot injection method

Fig. 1 illustrates the step-by-step schematic diagram of the synthesis process for FAPbBr₃ QDs. The preparation begins with the Formamidinium (FA) solution, where 0.521 g of methyl ether acetate is added to 10 mL of oleic acid (OA) and degassed at 100 °C for 30 min. The temperature is then increased to 120 °C for another 30 min before being maintained at 80 °C under a nitrogen (N₂) atmosphere for 1 hour, resulting in what we refer to as the FA-OA solution. To introduce the ligand structure, didodecyldimethylammonium bromide (DDAB) is dissolved in a mixture of 4 mL of toluene (Tol) and Oleylamine (OAm) through ultrasonication until fully dissolved. Then the PbBr₂ solution is prepared by dissolving 0.135 g of PbBr₂ in 10 mL of octadecene (ODE) and degassing at 120 °C for 2 h to remove water and oxygen. Following this, 1 mL of OA and 0.5 mL of OAm are added under a nitrogen atmosphere, and the solution is heated to 190 °C until all the components are completely dissolved. When the temperature reaches 190 °C, 1 mL of the FA-OA solution is injected, and the mixture is allowed to cool to room temperature. Subsequently, the DDAB ligand solution is injected and allowed to react for 5 min. The resulting mixture is then quickly quenched in an ice bath for 10 s, and the FAPbBr₃ solution is collected. This solution is centrifuged at 8000 rpm for 10 min, followed by the addition of 10 mL of hexane (Hex). The centrifugation process is repeated for another 10 min, and the supernatant is collected. Next, 10 mL of ethyl acetate (EtOAc) is added, and the centrifugation is repeated. The final FAPbBr₃ precipitate is then dispersed in n-octane (Oct) at a concentration of 160 mg/ml and stored at 4 °C. We prepared four different samples by varying the molar concentration of DDAB during synthesis: 0 mmol, 0.1 mmol, 0.2 mmol, and 0.3 mmol, referred to as DDAB*0, DDAB*1, DDAB*2, and DDAB*3, respectively.

2.2. Device fabrication of the QPDs utilizing FAPbBr₃ QDs

The indium tin oxide (ITO) substrates were initially cleaned ultrasonically using deionized water, absolute ethanol, and acetone. Following this, they were treated with UV-ozone for 15 min to remove any adsorbed organic matter and enhance surface hydrophilicity. Next, PCBM powder, dissolved in chlorobenzene at 40 mg/ml, was spin-

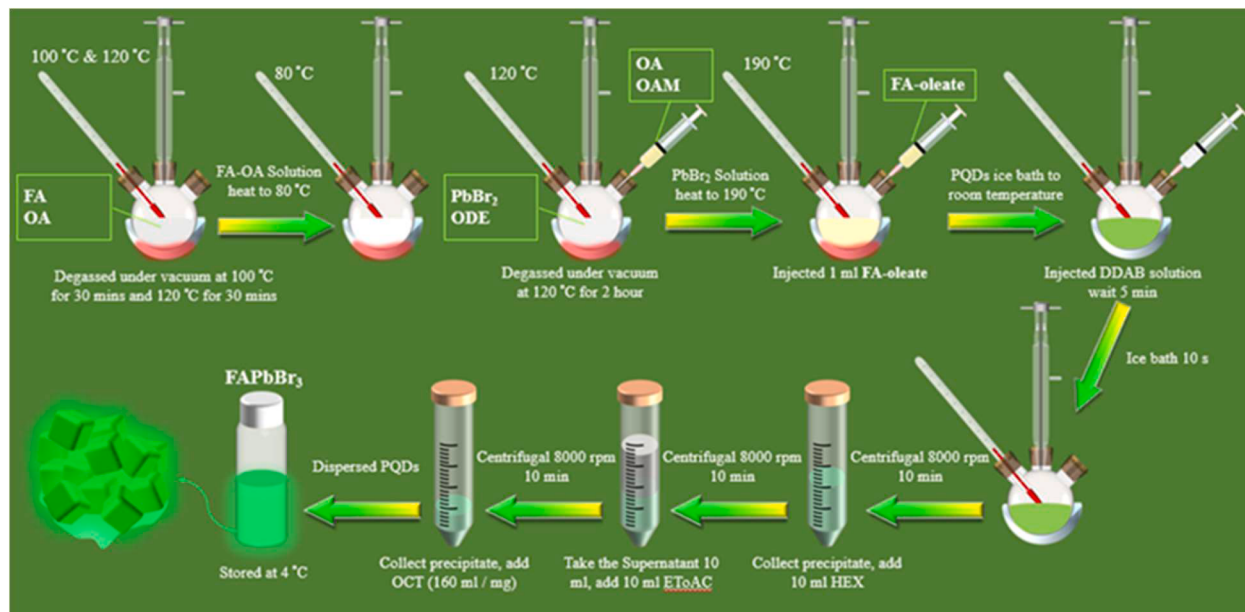


Fig. 1. Schematic representation of the preparation process for FAPbBr_3 QDs. The diagram illustrates the step-by-step synthesis procedure, highlighting key stages in forming the QDs.

coated onto the ITO at 3000 rpm for 30 s to ensure uniform coverage, followed by thermal annealing at 100 °C for 10 min. The green FAPbBr_3 QDs, dissolved in n-octane, were then spin-coated at 3000 rpm on PCBM. Finally, 1,1-bis((di-4-tolylamino)phenyl)cyclohexane (TAPC), Molybdenum(VI) Oxide MoO_3 , and Silver (Ag) were evaporated sequentially using a three-source evaporation system, maintaining a chamber pressure below 5E^{-2} torr and depositing layer thicknesses of 100 nm, 10 nm, and 100 nm, respectively. Four types of devices ITO/PCBM/QDs-DDAB (DDAB*0, DDAB*1, DDAB*2, and DDAB*3)/TAPC/ MoO_3 /Ag were fabricated for comparison purposes. The materials and device characterizations are provided in the supplementary file.

3. Results and discussion

3.1. Analysis of material characterization of FAPbBr_3 QDs with different DDAB concentrations

Fig. 2 (a, b) shows the photo of the irradiation of the light with and without UV lamp respectively of FAPbBr_3 QDs samples with different concentration of DDAB (DDAB*0, DDAB*1, DDAB*2, and DDAB*3). Upon UV light irradiation, a noticeable change in color was observed across all samples, shifting from yellow-green to a bright green. This clearly demonstrates that the samples emit green light when exposed to UV radiation. The absorption and photoluminescence spectra of the different mole ratio of the DDAB are seen and observed the luminance

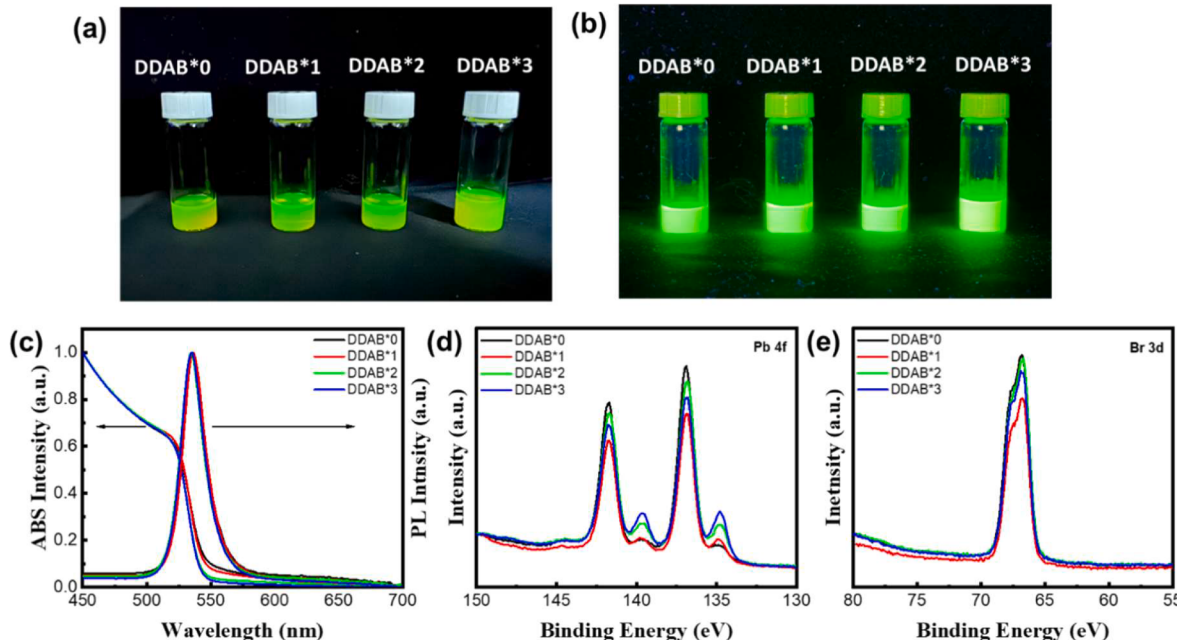


Fig. 2. (a, b) Digital photographs showing the sample under UV lamp and without UV lamp exposure. (c) absorption and photoluminescence spectra and (d, e) XPS spectra illustrating the Pb 4f and Br 3d core levels with different DDAB (DDAB*0, DDAB*1, DDAB*2, and DDAB*3) concentrations.

spectra at the wavelength of 550 nm. When adding the different ligand concentration, all the absorbance spectra were observed at the wavelength of 525 nm (Fig. 2c). Additionally, the FAPbBr₃ QDs with all the molar concentration consistently maintain their PL emission above 520 nm, enabling the achievement of pure green color in the National Television Standards Committee (NTSC) chromaticity diagram [57,58]. The strong green PL emission of FAPbBr₃ QDs with difference concentrations are primarily attributed to exciton recombination, which aligns well with findings reported in other studies [20,59,60].

The XPS analysis presented in Fig. 2(d) and 2(e) shows that the Pb 4f and Br 3d peaks offer valuable information about the valence states of lead and bromine in FAPbBr₃ QDs. The Pb 4f_{7/2} and Pb 4f_{5/2} peaks, located at approximately 138 eV and 143 eV, respectively, are consistent across varying concentrations of DDAB (DDAB*0, DDAB*1, DDAB*2, and DDAB*3) [61,62]. Likewise, the Br 3d peak is observed at 67.5 eV. These results confirm that surface passivation with DDAB does not alter the intrinsic Pb-Br chemical bonds, thus preserving the material's stability and integrity across different DDAB concentrations. This binding energy aligns with previously reported values for Br in lead halide perovskites, confirming that the passivation process preserves the perovskite's chemical structure without disrupting the core Pb-Br bonds. The Pb 4f and Br 3d results further demonstrate the integrity of the Pb-Br bonds in FAPbBr₃ QDs across varying DDAB concentrations (DDAB*0, DDAB*1, DDAB*2, and DDAB*3) [63,64].

TEM images of FAPbBr₃ QDs without and with different DDAB (DDAB*0, DDAB*1, DDAB*2, and DDAB*3) concentrations are shown in Fig. 3, with the increase of concentration, the particle size does not change much, and it is observed at the range of 13 nm. Additionally, the TEM images show slight nanocrystal agglomeration when 0.3 mmol of DDAB is added, likely due to an excess of ligands. In contrast, at a concentration of 0.2 mmol, the nanocrystals exhibit good monodispersity with an average size of 13.04 nm, which is smaller compared to those formed at other DDAB concentrations.

To analyze the crystal phase and its changes with varying ligand concentrations, XRD measurements were performed, as shown in Fig. 4(a). The XRD data for the FAPbBr₃ perovskite QDs shows the diffraction peaks observed at 15°, 21.2°, 30°, and 33.6° correspond to the (100), (110), (200), and (210) planes of the cubic FAPbBr₃ crystal with a Pm3̄m space group [65,66]. No significant additional diffraction peaks were observed in the XRD patterns [67]. With increasing DDAB concentration, a slight broadening of the peaks was detected, likely due to a

variation in crystal size. In the synthesis process without DDAB ligands (DDAB*0), surface defects are introduced, and long-chain OA and OAm ligands remain attached to the perovskite crystal surface. However, these long-chain ligands are replaced by the short-chain DDAB during ligand substitution. This modification not only provides excess bromide ions, reducing surface defects and shortening the nanocrystals, but also enhances carrier transport efficiency.

Proceed to Fig. 4(b), the changes of surface ligands after DDAB modification of FAPbBr₃ QDs can be confirmed by FTIR. From this spectrum, the N-H stretching vibration at 3270 cm⁻¹ in FA⁺ organic compound [68], the C-H bond at 2850 cm⁻¹, 2920 cm⁻¹, and the C-N symmetric stretching of FA cations at 1715 cm⁻¹ can be observed without DDAB [69]. When the concentration is increased to 0.2 mmol (DDAB*2) and 0.3 mmol (DDAB*3), the C-H, C=O, and N-H bonds become undetectable, indicating that the long-chain methylene groups from the organic compound have significantly diminished. This confirms that DDAB has been successfully passivated on the surface of the perovskite QDs [70]. For FAPbBr₃ quantum dots, the bending vibrations of C=C observed at 908 cm⁻¹ and 750 cm⁻¹ confirm the presence of the surface capping ligand, indicating successful passivation of the quantum dots [71]. The ionic bonding properties in PQDs make the binding between ligands and QDs highly dynamic, which replaces OA and OAm ligands, thereby avoiding the formation of surface vacancies and defects.

The SEM (Fig. 4c) and AFM (Fig. 4d) images illustrate the influence of DDAB concentration on the surface morphology and roughness of FAPbBr₃ QDs on PCBM. As DDAB concentration increases, the surface coverage of QDs improves due to enhanced interaction with the electron transport layer (ETL) [32]. However, at a concentration of 0.3 mmol, significant hole formation occurs in the film, which can increase leakage current and impair carrier transport. The AFM results indicate that the surface roughness (R_a) is relatively high at 5.37 nm without DDAB but decreases significantly to 2.34 nm at 0.2 mmol DDAB concentration (with R_a values of 5.37 nm at 0.1 mmol and 3.99 nm at 0.3 mmol), indicating a smoother and more uniform film. This smoother surface improves adhesion between the PQDs and the underlying film, contributing to enhanced film uniformity. The contact angle measurements (Fig. 4e) demonstrate the different concentrations of DDAB ligands used to passivate the FAPbBr₃ QDs surface. Wettability, whether hydrophilic or super hydrophilic, is determined by the contact angle, with values greater than 10° (but <90°) indicating hydrophilicity and values below 10° indicating superhydrophilicity [72]. The increased surface hydrophilicity with 0.2 mmol of DDAB can be attributed to the

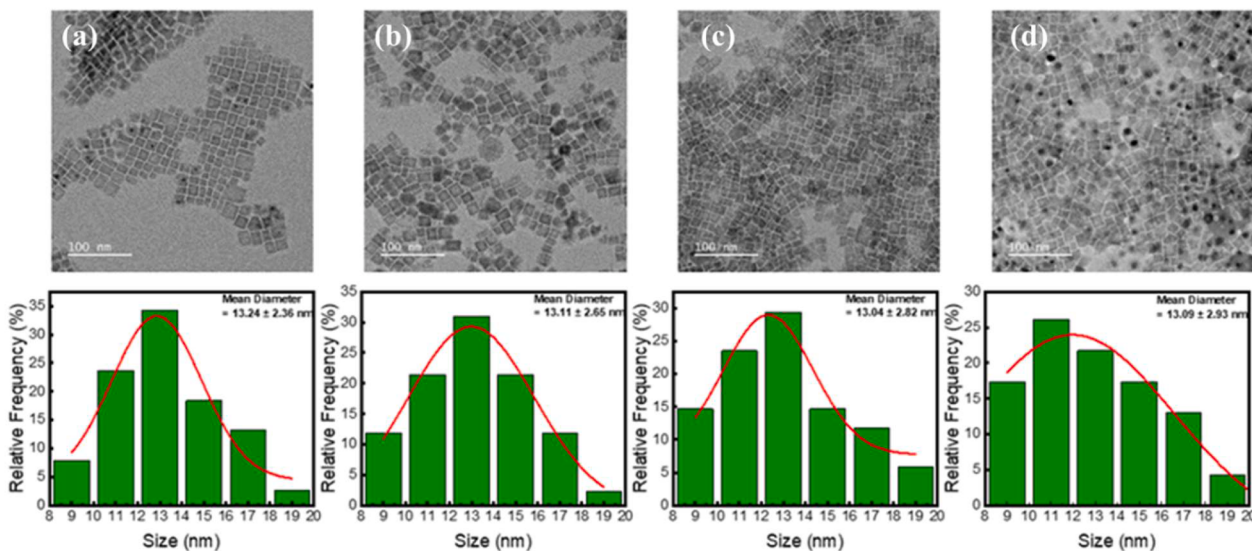


Fig. 3. TEM images and particle size analysis of FAPbBr₃ QDs synthesized under varying concentrations of DDAB ((a) DDAB*0, (b) DDAB*1, (c) DDAB*2, and (d) DDAB*3). The figure illustrates the impact of DDAB concentration on the morphology and size distribution of the QDs.

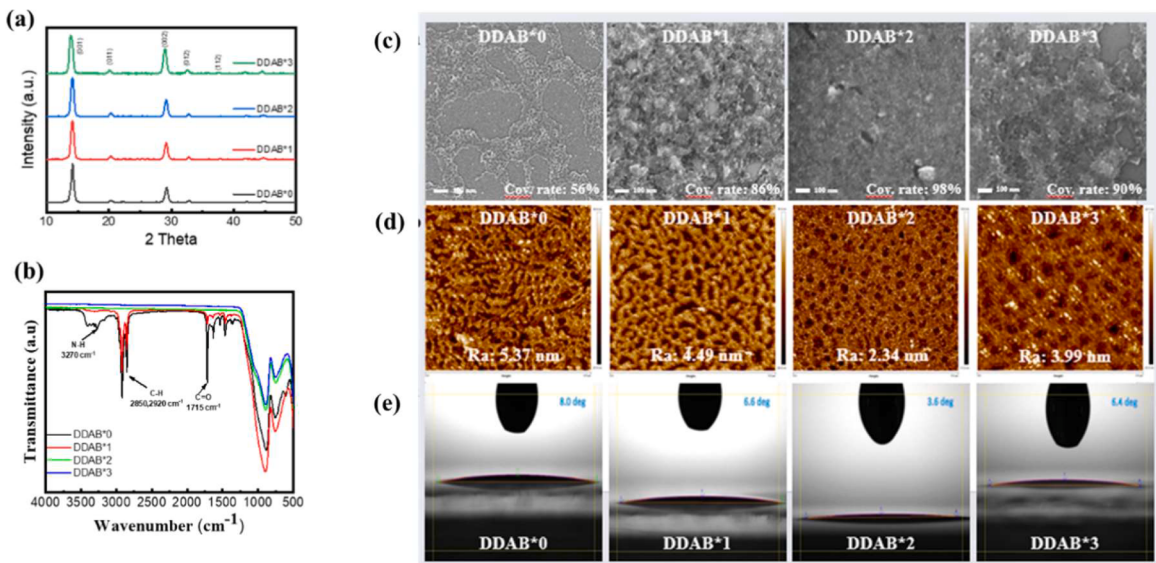


Fig. 4. Comprehensive characterization of FAPbBr₃ QDs synthesized with different concentrations of DDAB, including their corresponding (a) XRD patterns, (b) FTIR spectra, (c) SEM images, (d) AFM images, and contact angle measurements.

molecular structure of DDAB. DDAB contains a hydrophilic head and hydrophobic alkyl chains, which interact with the surface of the PQDs. In the absence of DDAB passivation, the FAPbBr₃ QDs exhibit a contact angle of 8.0°, indicating significant hydrophilicity (Fig. 4b). After passivation with DDAB ligands, the contact angle decreases further to 3.6°, suggesting an increase in surface hydrophilicity. This enhanced hydrophilicity, facilitated by DDAB, helps in reducing surface defect states and potentially improving the overall performance of the FAPbBr₃ QDs by passivating surface traps and enhancing stability.

The Time resolved photoluminescence spectroscopy (TRPL) (Fig. 5) results demonstrate that the addition of DDAB increases the carrier lifetime of FAPbBr₃ QDs as shown in Table 1. Here, we use a biexponential model to fit the emission decay curve of our sample, as described by the equation:

Table 1
Carrier life time of the FAPbBr₃ with different concentration of DDAB.

TRPL	A ₁	τ ₁ (ns)	A ₂	τ ₂ (ns)	τ _{av} (ns)	R ²
DDAB*0	69,727.711	26.85	2311.970	69.67	30.24	1
DDAB*1	38,380.224	36.01	2872.592	90.33	44.60	0.99999
DDAB*2	24,551.192	49.19	2780.417	120.20	64.58	0.99999
DDAB*3	35,674.294	36.45	2913.079	91.38	45.78	0.9999

$$I(t) = A_1 \exp(-t / \tau_1) + A_2 \exp(-t / \tau_2)$$

The equation contained both the fast (short-lifetime time constant τ_1 and amplitude constant A_1) and slow (long-lifetime time constant τ_2 and amplitude constant A_2) components, where the short value represented

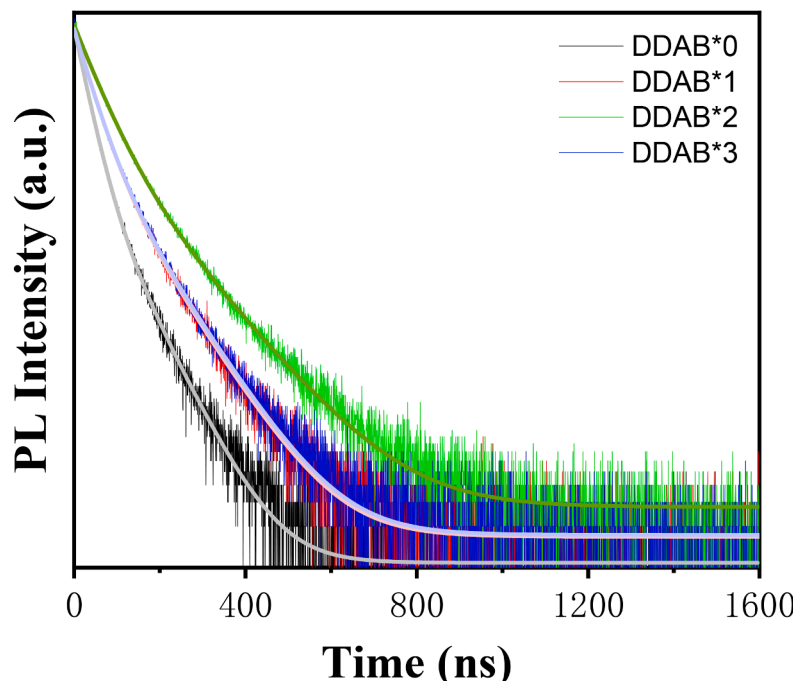


Fig. 5. TRPL and the fitting data of FAPbBr₃ QDs with different concentrations of DDAB.

the existence of defect state to trap carriers and the long value reflected the radiative recombination of carrier [73]. And τ_{avg} refers to the amplitude-weighted average lifetimes, which can be given by the equation below

$$\tau_{\text{avg}} = (A_1 \tau_1^2 + A_2 \tau_2^2) / (A_1 \tau_1 + A_2 \tau_2)$$

The obtained R^2 values (coefficient of determination) were very close to 1 (Table 1), which gives us strong confidence that this model is appropriate. In the cases of DDAB*0 and DDAB*1, the long-chain ligands OA and OAM are attached to the QD surface, resulting in reduced average carrier lifetimes of 30.24 ns and 44.60 ns, respectively. The

highest average lifetime (τ_{avg}) of 64.58 ns was observed at DDAB*2, which decreased to 45.78 ns at DDAB*3. The shorter lifetime observed in DDAB*3 suggests a higher trap density due to suboptimal crystal conditions, while the longer lifetime in DDAB*2 indicates more efficient carrier transport across the crystal surface, with fewer defects [74]. This suggests that DDAB*2 will likely lead to better device performance than other DDAB concentrations. Furthermore, the extended lifetime enhances electron-hole pair separation, promoting charge carrier transport and reducing the likelihood of Auger and non-radiative recombination [28,75]. The suppressed non-radiative recombination in DDAB*2, which exhibited the longest decay lifetime among all concentrations, not only

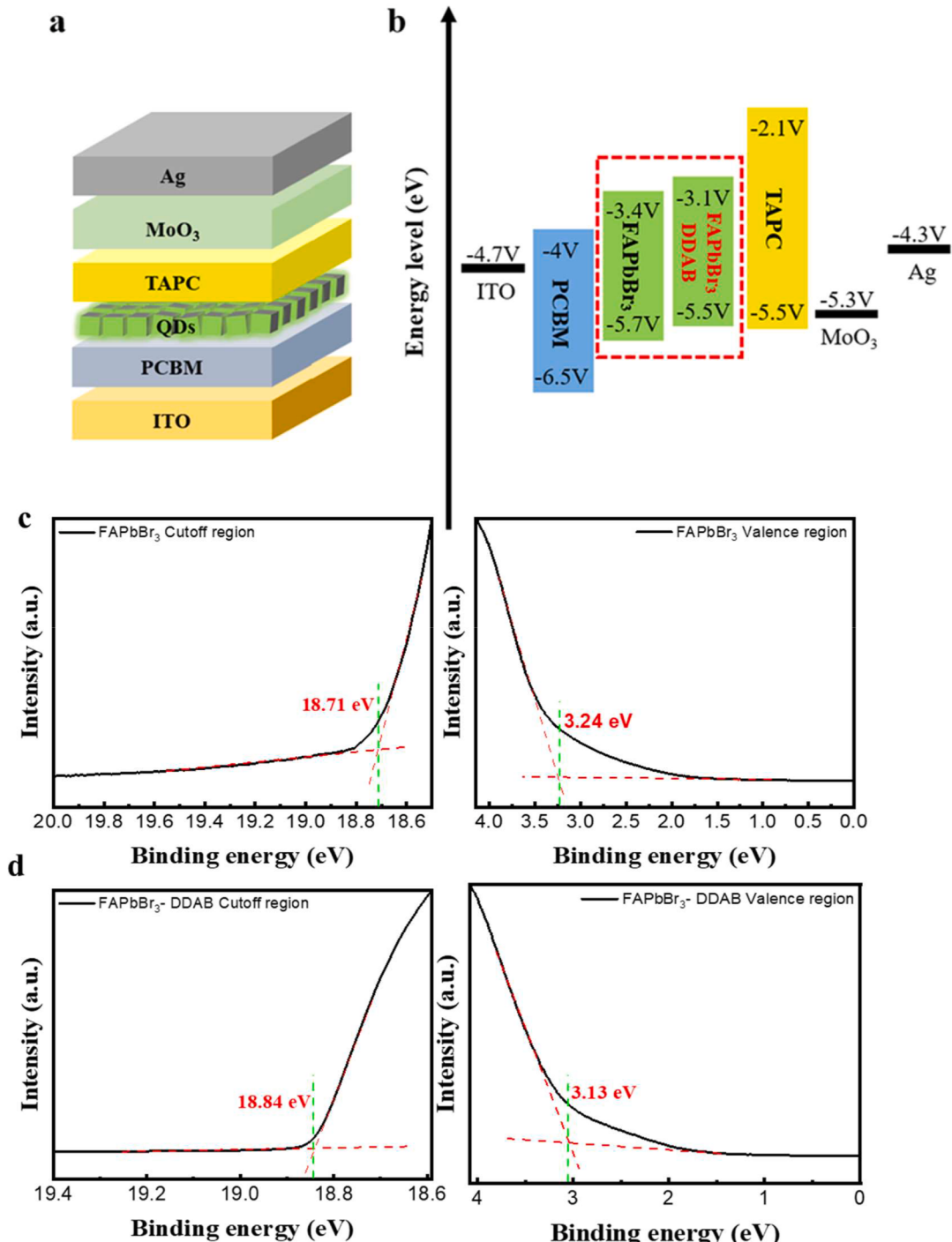


Fig. 6. (a) Schematic diagram of the structure of the QPDs and their (b) energy level diagram of each layer of materials. UPS measurement of (c) FAPbBr₃ and (d) FAPbBr₃-DDAB*2 with the cutoff and valence region.

improves stability but also indicates more efficient charge carrier transport to photoconductive active sites, positioning it as a promising candidate for advancing optoelectronic applications [68].

Next, we fabricated devices based on the structure ITO/PCBM/FAPbBr₃ QDs DDAB (with and without DDAB*2) /TAPC/MoO₃/Ag (Fig. 6(a)) and analyzed their energy level diagrams, as shown in Fig. 6(b). The HOMO and LUMO energy levels for FAPbBr₃ and FAPbBr₃/DDAB*2 were determined from UPS spectra (Fig. 6(c&d)) and calculated using Eq. (1) as follows.

$$E_g(\text{Energy gap}) \cong \frac{1240}{\lambda(\text{wavelength})} \rightarrow \lambda(\text{wavelength}) \cong \frac{1240}{E_g} \quad (1)$$

The energy gap (E_g) was estimated from an absorption wavelength of about 530 nm, yielding HOMO levels of -5.7 eV and -5.5 eV, and LUMO levels of -3.4 eV and -3.1 eV for FAPbBr₃ and FAPbBr₃/DDAB*2, respectively. Notably, the LUMO energy level of FAPbBr₃/DDAB*2 showed better alignment with TAPC (5.5 eV), facilitating more efficient electronic transitions, as detailed in Table S1. To verify that carrier migration speed is minimally affected by energy level shifts, we fabricated single-carrier devices to measure hole mobilities. The results showed hole mobilities of 7.85×10^{-5} cm²/Vs without DDAB passivation and 8.31×10^{-4} cm²/Vs with DDAB*2 passivation, indicating a slight increase in migration speed after ligand replacement.

The EQE performance of devices with FAPbBr₃ and FAPbBr₃/DDAB*2 at 530 nm was observed to be 10.1 % and 26.94 %, respectively, as shown in Fig. 7(a). Fig. 7(b) presents the dark current measurements, with values of 5.84×10^{-6} A/cm² for FAPbBr₃ and 3.31×10^{-7} A/cm² for FAPbBr₃-DDAB*2 at -1 V, indicating that the dark current is significantly reduced with the addition of the DDAB*2 ligand. At 0 V, the dark current values were 2.85×10^{-10} A/cm² and 1.04×10^{-11} A/cm² for FAPbBr₃ and FAPbBr₃-DDAB*2, respectively, showing further reduction after ligand modification. This substantial decrease in dark current density for FAPbBr₃-DDAB*2 devices suggests improved

charge transport properties in the FAPbBr₃ PQD films. Theoretically, this improvement can be attributed to the shortened and more ordered charge transport paths between neighboring QDs in the DDAB*2-treated films, caused by the partial substitution of the long-chain ligands with the shorter DDAB ligands. Fig. 7(c) shows the spectral responsivity (SR) at 530 nm, with values of 0.04 A/W for FAPbBr₃ and 0.08 A/W for FAPbBr₃-DDAB*2. The SR, defined as the ratio of photogenerated current density to input optical power density, can be calculated using Eq. (2).

$$\begin{aligned} \text{SR}(\lambda) &= \frac{\text{photo-generated current density}}{\text{input light power density}} = \frac{EQE(\lambda) \times q \times \lambda}{hc} \\ &= \frac{EQE(\lambda) \times q}{hv} = \frac{EQE(\lambda) \times \lambda}{1240} \end{aligned} \quad (2)$$

where h is Planck's constant, c is the speed of light, hv is the photon frequency, q is the electron charge, and λ is the wavelength of the incident light. Using the SR obtained from Eq. (2) and applying it to Eq. (3), the detectivity (D^*) can be determined [76].

$$D^* = \frac{q\lambda\sqrt{AB} \times EQE(\lambda)}{i \times hc} = \frac{SR(\lambda)\sqrt{AB}}{i} \quad (3)$$

where A for the module area, B for the bandwidth, and i for the dark current.

Fig. 7(d) presents the D^* of the QPDs based on FAPbBr₃ and FAPbBr₃-DDAB*2 at 530 nm, assessing the optoelectronic performance of the devices. The D^* values for the un-passivated and DDAB-passivated QPDs were 1.13×10^{11} Jones and 7.93×10^{12} Jones, respectively. As expected, the detection capability of the device significantly improved with the addition of the DDAB*2 ligand. This substantial increase in D^* can be attributed to the reduced dark current and enhanced spectral responsivity following DDAB passivation, as shown in Fig. 7(b) and 7(c).

Fig. 8 illustrates the LDR, a key indicator of QPDs performance,

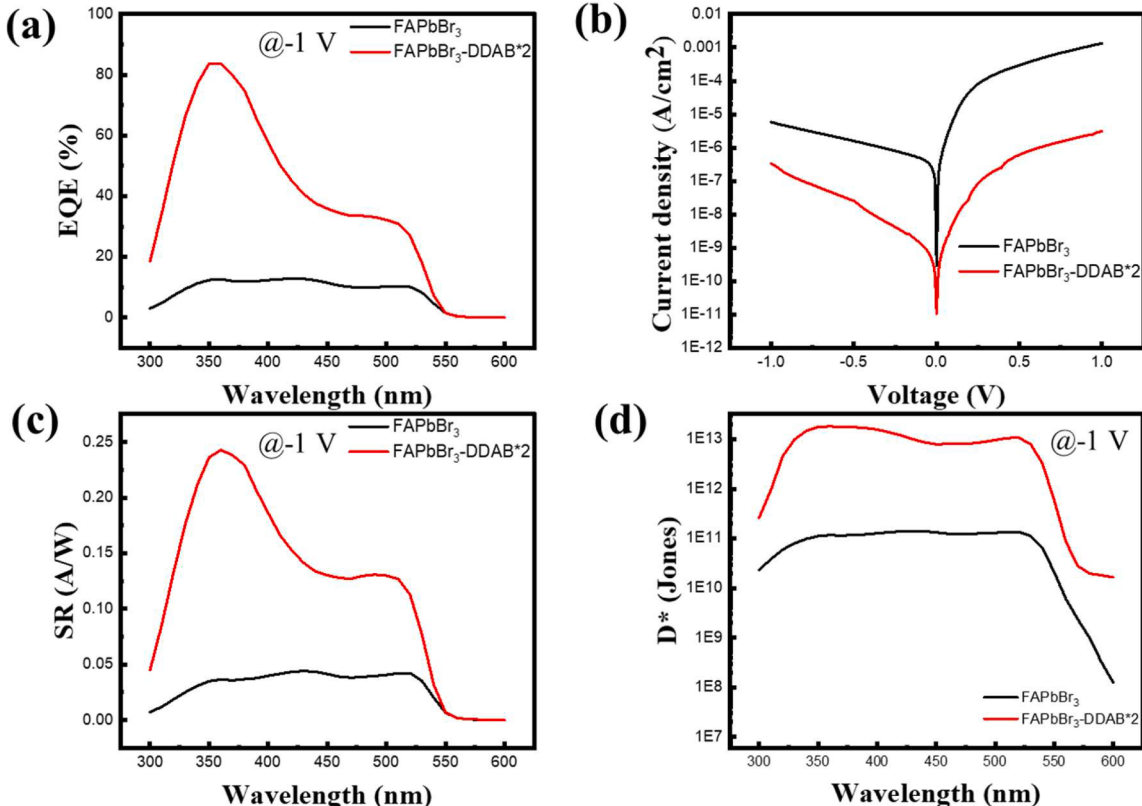


Fig. 7. (a) EQE (b) Dark current J-V (c) Spectral response (SR) (d) Sensitivity (D^*) of FAPbBr₃ and FAPbBr₃-DDAB for photo detector.

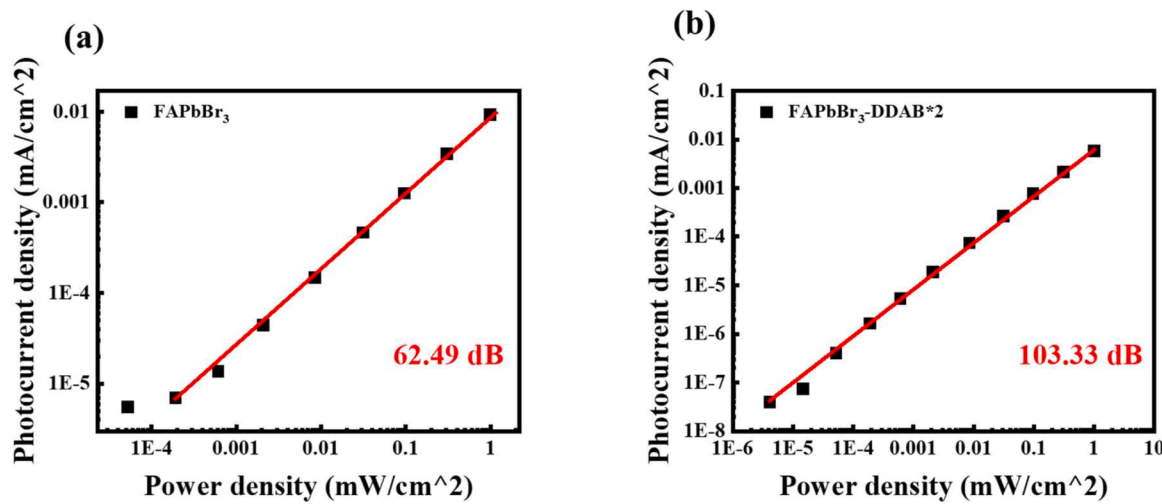


Fig. 8. LDR of (a) FAPbBr₃ and (b) FAPbBr₃-DDAB*2 for QPDs device.

which is calculated based on the correlation between the photocurrent under varying light intensities and the change in responsivity using Eq. (4)

$$LDR = 20 \log \frac{P_{max}}{P_{min}} \quad (4)$$

P_{max} is the maximum incident photocurrent density and P_{min} is the minimum incident photocurrent density. Under 530 nm illumination, the LDR values for FAPbBr₃ and FAPbBr₃-DDAB*2 were 62.49 dB and 103.33 dB, respectively. Fig. S1 shows the time response of the QPDs, measured under green LED irradiation at a wavelength of 530 nm, with a fixed intensity of 1 mW and a flicker frequency of 1 kHz. The rise time (t_{rise}) and fall time (t_{fall}) corresponding to the time required for the photocurrent to increase from 10 % to 90 % and decrease from 90 % to 10 %, are shown in Table S3. The QPDs without DDAB exhibited t_{rise} of 163.87 μ s and t_{fall} of 92.02 μ s, while those with DDAB*2 showed significantly faster times of 3.64 μ s and 1.97 μ s, respectively. Furthermore, Fig. S2 presents the frequency response of the module, indicating that the -3 dB cut-off frequency (f_{-3} dB) the point where the power output drops to half of the maximum was 3 kHz for FAPbBr₃ and 49 kHz for FAPbBr₃-DDAB*2. This demonstrates that the addition of DDAB ligands significantly optimized the module's performance of the QPDs.

Table 2 presents a performance comparison of various device structures based on QPDs with different DDAB (DDAB*0, DDAB*1, DDAB*2, and DDAB*3) passivation. Key metrics, including EQE, J_d , D^* , LDR, on/off response times, and cut-off frequency, are reported for each configuration. The best-performing device, ITO/PCBM/QDs-DDAB*2/TAPC/MoO₃/Ag, achieved the highest EQE (26.94 %), detectivity (up to 1.78×10^{13} Jones), and LDR (103.33 dB), along with superior on/off response times compared to the pure FAPbBr₃ QDs. Additionally, this device exhibited a cut-off frequency of 49 kHz, indicating an excellent high-frequency response, while the pure FAPbBr₃ QDs device had a

significantly lower cut-off frequency of 3 kHz. It is well-known that longer ligands, such as OA and OAm, are commonly used for surface passivation and excess ligands can hinder nucleation and lead to QDs degradation. The weak binding of OA and OAm to the QDs surface can result in ligand loss, causing the formation of surface defects, such as halide vacancies, which promote QD agglomeration and increase surface energy and defect density. In contrast, the long-term stability of our DDAB*2-capped QDs demonstrates that DDAB ligands provide stronger binding, enhancing both the optical and phase stability of perovskite QDs.

4. Conclusions

In this study, surface passivation and ligand exchange of FAPbBr₃ QDs using DDAB were investigated to optimize their performance in QPDs. FAPbBr₃ precursor solutions with varying DDAB concentrations were synthesized via hot injection method. These materials were characterized using XPS, XRD, FTIR, SEM and TEM and other analytical techniques, confirming that DDAB passivation effectively replaced the OA and OAm short-chain ligands, reducing surface defects in the perovskite nanocrystals and enhancing their structural stability and optoelectronic properties. The experimental results show that, at a wavelength of 530 nm, DDAB*2-passivated FAPbBr₃ PQDs achieved an EQE of 26.94 %, with D^* increased to 7.93×10^{12} Jones, an LDR of 103.33 dB, and significantly faster response times, with rise and fall times reduced to 3.64 μ s and 1.97 μ s, respectively. Frequency response tests further demonstrated that the -3-dB cut-off frequency was increased to 49 kHz after DDAB passivation, indicating a much faster response. In conclusion, DDAB ligand exchange and surface passivation significantly improved the optoelectronic performance of FAPbBr₃ QDs, highlighting their potential for use in high-efficiency photodetectors and optoelectronic sensors.

Table 2

Opto-electronic performance of QPDs device with differ concentration of DDAB (DDAB*0, DDAB*1, DDAB*2, and DDAB*3) ligands.

Devices structure	EQE (530nm)	J_d (0v&-1v)	D^* (530nm & 350nm)	LDR (dB)	On/Off (μ s)	Cut off (Hz)
ITO/PCBM/Pure QDs/TAPC/MoO ₃ /Ag	10.1	2.85E-10 5.84E-6	1.13E11 1.12E11	62.49	t_{rise} :163.87 t_{fall} :92.02	3k
ITO/PCBM/QDs - DDAB*1/TAPC/MoO ₃ /Ag	15.51	1.78E-9 8.44E-7	1.75E11 3.68E11	84.81	t_{rise} :11.43 t_{fall} :9.68	25k
ITO/PCBM/QDs - DDAB*2/TAPC/MoO ₃ /Ag	26.94	1.04E-11 3.31E-7	7.98E12 1.78E13	103.33	t_{rise} :3.64 t_{fall} :1.97	49k
ITO/PCBM/QDs - DDAB*3/TAPC/MoO ₃ /Ag	23.89	1.06E-9 4.89E-7	3.99E11 8.17E11	98.36	t_{rise} :11.99 t_{fall} :10.19	23k

CRediT authorship contribution statement

Wei-Kuan Hung: Validation, Project administration, Formal analysis, Conceptualization. **Kasimayan Uma:** Writing – original draft, Validation, Methodology, Data curation. **Shu-Meng Yang:** Writing – review & editing, Validation, Formal analysis. **Lung-Chien Chen:** Writing – review & editing, Supervision, Investigation, Formal analysis, Conceptualization. **Yu-Cheng Lin:** Writing – review & editing, Visualization, Formal analysis. **Zong-Liang Tseng:** Writing – review & editing, Supervision, Project administration, Investigation, Funding acquisition, Data curation, Conceptualization.

Declaration of competing interest

The authors declare that they have no known competing financial interests or personal relationships that could have appeared to influence the work reported in this paper.

Acknowledgement

The authors would like to thank the National Science and Technology Council for financial support through grant number NSTC 112-2221-E-131-022-MY3.

Supplementary materials

Supplementary material associated with this article can be found, in the online version, at [doi:10.1016/j.rineng.2025.104693](https://doi.org/10.1016/j.rineng.2025.104693).

Data availability

Data will be made available on request.

References

- [1] Z. Zhao, C. Xu, L. Niu, X. Zhang, F. Zhang, Recent progress on broadband organic photodetectors and their applications, *Laser Photonics Rev* 14 (2020) 1–24, <https://doi.org/10.1002/lpor.202000262>.
- [2] R.D. Jansen-van Vuuren, A. Armin, A.K. Pandey, P.L. Burn, P. Meredith, Organic photodiodes: the future of full color detection and image sensing, *Adv. Mater.* 28 (2016) 4766–4802, <https://doi.org/10.1002/adma.201505405>.
- [3] X. Qiu, Y. Ding, Z. Sun, H. Ji, Y. Zhou, Z. Long, G. Liu, P. Wang, S. Poddar, B. Ren, K. Zhou, Z. Li, Y.B. Cao, Z. Ma, B. Li, Y. Lin, B. Huang, J. Wang, H.S. Kwok, Z. Fan, A tetrachromatic sensor for imaging beyond the visible spectrum in harsh conditions, *Device* 2 (2024) 100357, <https://doi.org/10.1016/j.device.2024.100357>.
- [4] T. Yaseen Ahmed, S.B. Aziz, E.M.A. Dannoun, Role of outer shell electron-nuclear distant of transition metal atoms (TMA) on band gap reduction and optical properties of TiO₂ semiconductor, *Results Eng.* 23 (2024) 102479, <https://doi.org/10.1016/j.rineng.2024.102479>.
- [5] S.N. Backer, S.E. Oussadou, I.W. Almanassra, M. Khairi Mousa, M.A. Atieh, A. Shanableh, Effect of energy band alignments in carbon doped ZnO/TiO₂ hybrid heterojunction photocatalyst on the photodegradation of ofloxacin, *Results Eng.* 20 (2023) 101432, <https://doi.org/10.1016/j.rineng.2023.101432>.
- [6] E.T. Wahyuni, S. Annur, N.D. Lestari, M. Mudasir, Conversion of iron rusty waste into Fe dopant of TiO₂ to increase its photocatalytic activity under visible light for photodegradation of rhodamine-B, *Results Eng.* 22 (2024) 102296, <https://doi.org/10.1016/j.rineng.2024.102296>.
- [7] E.T. Wahyuni, N.P. Diantariani, I. Kartini, A. Kuncaka, Enhancement of the photostability and visible photoactivity of ZnO photocatalyst used for reduction of Cr(VI) ions, *Results Eng.* 13 (2022) 100351, <https://doi.org/10.1016/j.rineng.2022.100351>.
- [8] M. Ahmadi, T. Wu, B. Hu, A review on organic–inorganic halide perovskite photodetectors: device engineering and fundamental physics, *Adv. Mater.* 29 (2017) 1–24, <https://doi.org/10.1002/adma.201605242>.
- [9] F. Wang, X. Zou, M. Xu, H. Wang, H. Wang, H. Guo, J. Guo, P. Wang, M. Peng, Z. Wang, Y. Wang, J. Miao, F. Chen, J. Wang, X. Chen, A. Pan, C. Shan, L. Liao, W. Hu, Recent progress on electrical and optical manipulations of perovskite photodetectors, *Adv. Sci.* 8 (2021) 1–15, <https://doi.org/10.1002/advs.202100569>.
- [10] W. Tian, H. Zhou, L. Li, Hybrid organic–inorganic perovskite photodetectors, *Small* 13 (2017), <https://doi.org/10.1002/smll.201702107>.
- [11] D. Ghosh, S. Kapri, S. Bhattacharyya, Phenomenal ultraviolet photoresponsivity and detectivity of graphene dots immobilized on zinc oxide nanorods, *ACS Appl. Mater. Interfaces* 8 (2016) 35496–35504, <https://doi.org/10.1021/acsmami.6b13037>.
- [12] A. Subramanian, J. Akram, S. Hussain, J. Chen, K. Qasim, W. Zhang, W. Lei, High-performance photodetector based on a graphene quantum dot/CH₃NH₃PbI₃ perovskite hybrid, *ACS Appl. Electron. Mater.* 2 (2020) 230–237, <https://doi.org/10.1021/acsaelm.9b00705>.
- [13] D. Li, J. Shi, Y. Xu, Y. Luo, H. Wu, Q. Meng, Inorganic–organic halide perovskites for new photovoltaic technology, *Natl. Sci. Rev.* 5 (2018) 559–576, <https://doi.org/10.1093/nsr/nwx100>.
- [14] T. Li, Y. Pan, Z. Wang, Y. Xia, Y. Chen, W. Huang, Additive engineering for highly efficient organic–inorganic halide perovskite solar cells: recent advances and perspectives, *J. Mater. Chem. A* 5 (2017) 12602–12652, <https://doi.org/10.1039/c7ta01798g>.
- [15] W. Li, Z. Wang, F. Deschler, S. Gao, R.H. Friend, A.K. Cheetham, Chemically diverse and multifunctional hybrid organic–inorganic perovskites, *Nat. Rev. Mater.* 2 (2017), <https://doi.org/10.1038/natrevmats.2016.99>.
- [16] J. Sun, J. Wu, X. Tong, F. Lin, Y. Wang, Z.M. Wang, Organic/inorganic metal halide perovskite optoelectronic devices beyond solar cells, *Adv. Sci.* 5 (2018), <https://doi.org/10.1002/advs.201700780>.
- [17] L. Gao, Y. Zhang, L. Gou, Q. Wang, M. Wang, W. Zheng, Y. Wang, H.L. Yip, J. Zhang, High efficiency pure blue perovskite quantum dot light-emitting diodes based on formamidinium manipulating carrier dynamics and electron state filling, *Light Sci. Appl.* 11 (2022), <https://doi.org/10.1038/s41377-022-00992-5>.
- [18] S. Zhou, Rapid separation and purification of lead halide perovskite quantum dots through differential centrifugation in nonpolar solvent, *RSC Adv.* 11 (2021) 28410–28419, <https://doi.org/10.1039/dra04578d>.
- [19] J. Ye, D. Gaur, C. Mi, Z. Chen, I. López Fernández, H. Zhao, Y. Dong, L. Polavarapu, R.L.Z. Hoye, Strongly-confined colloidal lead-halide perovskite quantum dots: from synthesis to applications, *Chem. Soc. Rev.* 53 (2024), <https://doi.org/10.1039/d4cs00077c>.
- [20] S. Iqbal, X. Duan, J. Wang, L. Liu, J.Y. Yang, Atomistic insight into the device engineering of inorganic halide perovskite solar cells, *Results Eng.* 24 (2024) 103105, <https://doi.org/10.1016/j.rineng.2024.103105>.
- [21] A.E. Magdalin, P.D. Nixon, E. Jayaseelan, M. Sivakumar, S.K.N. Devi, M.S. P. Subathra, N.M. Kumar, N. Ananthi, Development of lead-free perovskite solar cells: opportunities, challenges, and future technologies, *Results Eng.* 20 (2023) 101438, <https://doi.org/10.1016/j.rineng.2023.101438>.
- [22] H. Li, J. He, X. Wang, Q. Liu, X. Luo, M. Wang, J. Liu, C. Liu, Y. Liu, Synthesis of size-adjustable CsPbBr₃ perovskite quantum dots for potential photoelectric catalysis applications, *Materials (Basel)* 17 (2024), <https://doi.org/10.3390/ma17071607>.
- [23] L. Srathongsaian, A. Kaewprajak, A. Naikaew, C. Seri wattanachai, N. Phuphanaphong, A. Inna, T. Chotchuangchutchaval, W. Passatorntasachakorn, P. Kumornkaew, S. Sahasithiwat, D. Wongratanaaphisan, P. Ruankham, R. Supruangnet, H. Nakajima, P. Pakawatpanurut, P. Kanjanaboons, Cs and Br tuning to achieve ultralow-hysteresis and high-performance indoor triple cation perovskite solar cell with low-cost carbon-based electrode, *IScience* 27 (2024) 109306, <https://doi.org/10.1016/j.isci.2024.109306>.
- [24] I. Raifuku, Y. Ishikawa, Y.H. Chiang, P.Y. Lin, M.H. Li, Y. Uraoka, P. Chen, Segregation-free bromine-doped perovskite solar cells for IoT applications, *RSC Adv.* 9 (2019) 32833–32838, <https://doi.org/10.1039/c9ra05323a>.
- [25] K.A. Bush, K. Frohma, R. Prasanna, R.E. Beal, T. Leijtens, S.A. Swifter, M. D. McGehee, Compositional engineering for efficient wide band gap perovskites with improved stability to photoinduced phase segregation, *ACS Energy Lett.* 3 (2018) 428–435, <https://doi.org/10.1021/acsenergylett.7b01255>.
- [26] Q. Zhao, S. Wang, Y.H. Kim, S. Mondal, Q. Miao, S. Li, D. Liu, M. Wang, Y. Zhai, J. Gao, A. Hazarika, G.R. Li, Advantageous properties of halide perovskite quantum dots towards energy-efficient sustainable applications, *Green Energy Environ.* 9 (2024) 949–965, <https://doi.org/10.1016/j.gee.2023.04.001>.
- [27] D. Chen, X. Chen, Luminescent perovskite quantum dots: synthesis, microstructures, optical properties and applications, *J. Mater. Chem. C* 7 (2019) 1413–1446, <https://doi.org/10.1039/C8TC05545A>.
- [28] J. Jiao, C. Yang, Z. Wang, C. Yan, C. Fang, Solvent engineering for the formation of high-quality perovskite films:a review, *Results Eng.* 18 (2023) 101158. <https://doi.org/10.1016/j.rineng.2023.101158>.
- [29] A. Thankappan, A. Mayence, J. Jose, S. Thomas, Free standing organometallic dimethylammonium zinc formate perovskite for photonic and antimicrobial applications, *Results Eng.* 19 (2023) 1–9. <https://doi.org/10.1016/j.rineng.2023.101376>.
- [30] S. Dehsorkhi, M. Rbi, M. Monshi, M. Hosseinnezhad, Low turn-on voltage of doped organic light emitting diodes based on food dyes, *Results Eng.* 5 (2020) 100099. <https://doi.org/10.1016/j.rineng.2020.100099>.
- [31] M.M. Osman, Z. Almutairi, R. Almuzaiker, Effect of spin coating speeds on electrical and optical characteristic of perovskite SrTiO₃ thin films prepared by sol-gel method, *Results Eng.* 24 (2024) 103046. <https://doi.org/10.1016/j.rineng.2024.103046>.
- [32] M. Haneef, R.S. Almufaraj, S. Tahir, E. Gazo-Hanna, J. Arayro, E. Ali Shokralla, S. Hamed Alrefae, M. Abdelsabour Fahmy, R.R. Macadangdang, M.M. Saad H.E, A. Ashfaq, Optimization of a novel lead-free MASiI₃ based perovskite solar cell: a comprehensive study on device performance enhancement, *Results Eng.* 23 (2024) 102809, <https://doi.org/10.1016/j.rineng.2024.102809>.
- [33] Y.R. Park, S. Eom, H.H. Kim, W.K. Choi, Y. Kang, Self-defect-passivation by Br-enrichment in FA-doped Cs_{1-x}F_xPbBr₃ quantum dots: towards high-performance quantum dot light-emitting diodes, *Sci. Rep.* 10 (2020) 1–10, <https://doi.org/10.1038/s41598-020-71666-8>.

- [34] C. Li, Z. Zang, W. Chen, Z. Hu, X. Tang, W. Hu, K. Sun, X. Liu, W. Chen, Highly pure green light emission of perovskite CsPbBr_3 quantum dots and their application for green light-emitting diodes, Opt. Express 24 (2016) 15071, <https://doi.org/10.1364/oe.24.015071>.
- [35] T. Langer, A. Kruse, F.A. Ketzer, A. Schwiegel, L. Hoffmann, H. Jönen, H. Bremers, U. Rossow, A. Hangleiter, Origin of the “green gap”: increasing nonradiative recombination in indium-rich GaInN/GaN quantum well structures, Phys. Status Solidi Curr. Top. Solid State Phys. 8 (2011) 2170–2172, <https://doi.org/10.1002/pssc.201001051>.
- [36] A. Liu, A. Khanna, P.S. Dutta, M. Shur, Red-blue-green solid state light sources using a narrow line-width green phosphor, Opt. Express 23 (2015) A309, <https://doi.org/10.1364/oe.23.00a309>.
- [37] S. Baek, Y. Kim, S.W. Kim, Highly photo-stable CsPbI_3 perovskite quantum dots via thiol ligand exchange and their polymer film application, J. Ind. Eng. Chem. 83 (2020) 279–284, <https://doi.org/10.1016/j.jiec.2019.11.038>.
- [38] A.A. Al-Amriy, M.A. Fayad, H.A. Abdul Wahhab, W.K. Al-Azzawi, J.K. Mohammed, H.S. Majdi, Interfacial engineering for advanced functional materials: surfaces, interfaces, and applications, Results Eng. 22 (2024) 102125. <https://doi.org/10.1016/j.rineng.2024.102125>.
- [39] N. Fiua-Maneiro, K. Sun, I. López-Fernández, S. Gómez-Graña, P. Müller-Buschbaum, L. Polavarapu, Ligand chemistry of inorganic lead halide perovskite nanocrystals, ACS Energy Lett. 8 (2023) 1152–1191, <https://doi.org/10.1021/acsenergylett.2c02363>.
- [40] L. Li, W. Zheng, Q. Wan, M. Liu, Q. Zhang, C. Zhang, R. Yan, X. Feng, L. Kong, CsPbBr_3 nanocrystal light-emitting diodes with efficiency up to 13.4% achieved by careful surface engineering and device engineering, J. Phys. Chem. C 125 (2021) 3110–3118, <https://doi.org/10.1021/acs.jpcc.0c11085>.
- [41] Q. Xie, D. Wu, X. Wang, Y. Li, F. Fang, Z. Wang, Y. Ma, M. Su, S. Peng, H. Liu, K. Wang, X.W. Sun, Branched capping ligands improve the stability of cesium lead halide (CsPbBr_3) perovskite quantum dots, J. Mater. Chem. C 7 (2019) 11251–11257, <https://doi.org/10.1039/c9tc03377g>.
- [42] F. Zaccaria, B. Zhang, L. Goldoni, M. Imran, J. Zito, B. Van Beek, S. Lauciello, L. De Trizio, L. Manna, I. Infante, The reactivity of CsPbBr_3 Nanocrystals toward acid/base ligands, ACS Nano 16 (2022) 1444–1455, <https://doi.org/10.1021/acsnano.1c09603>.
- [43] W. Li, M. Hao, A. Baktash, L. Wang, J. Etheridge, The role of ion migration, octahedral tilt, and the A-site cation on the instability of $\text{Cs}_1\text{xFAxPbI}_3$, Nat. Commun. 14 (2023) 1–11, <https://doi.org/10.1038/s41467-023-44235-6>.
- [44] W. Fan, Q. Gao, X. Mei, D. Jia, J. Chen, J. Qiu, Q. Zhou, X. Zhang, Ligand exchange engineering of FAPbI_3 perovskite quantum dots for solar cells, Front. Optoelectron. 15 (2022) 1–12, <https://doi.org/10.1007/s12200-022-00038-z>.
- [45] S. Iqbal, X. Duan, J. Wang, L. Liu, J.Y. Yang, Atomistic insight into the device engineering of inorganic halide perovskite solar cells, Results Eng. 24 (2024) 103105. <https://doi.org/10.1016/j.rineng.2024.103105>.
- [46] F. Krieg, S.T. Ochsenbein, S. Yakunin, S. Ten Brinck, P. Aellen, A. Süess, B. Clerc, D. Guggisberg, O. Nazarenko, Y. Shynkarenko, S. Kumar, C.J. Shih, I. Infante, M. V. Kovalenko, Colloidal CsPbX_3 (X = Cl, Br, I) nanocrystals 2.0: zwitterionic capping ligands for improved durability and stability, ACS Energy Lett. 3 (2018) 641–646, <https://doi.org/10.1021/acsnenergylett.8b00035>.
- [47] X. Mei, K. He, R. Zhuang, M. Yu, Y. Hu, X. Zhang, Stabilizing dynamic surface of highly luminescent perovskite quantum dots for light-emitting diodes, Chem. Eng. J. 453 (2023), <https://doi.org/10.1016/j.cej.2022.139909>.
- [48] D. Yan, T. Shi, Z. Zang, T. Zhou, Z. Liu, Z. Zhang, J. Du, Y. Leng, X. Tang, Ultrastable CsPbBr_3 perovskite quantum dot and their enhanced amplified spontaneous emission by surface ligand modification, Small 15 (2019) 1–11, <https://doi.org/10.1002/smll.201901173>.
- [49] D. Jia, J. Chen, J. Qiu, H. Ma, M. Yu, J. Liu, X. Zhang, Tailoring solvent-mediated ligand exchange for CsPbI_3 perovskite quantum dot solar cells with efficiency exceeding 16.5%, Joule 6 (2022) 1632–1653, <https://doi.org/10.1016/j.joule.2022.05.007>.
- [50] J. Dai, J. Xi, Y. Zu, L. Li, J. Xu, Y. Shi, X. Liu, Q. Fan, J. Zhang, S.P. Wang, F. Yuan, H. Dong, B. Jiao, X. Hou, Z. Wu, Surface mediated ligands addressing bottleneck of room-temperature synthesized inorganic perovskite nanocrystals toward efficient light-emitting diodes, Nano Energy 70 (2020), <https://doi.org/10.1016/j.nanoen.2020.104467>.
- [51] H. Wu, Y. Zhang, M. Lu, X. Zhang, C. Sun, T. Zhang, V.L. Colvin, W.W. Yu, Surface ligand modification of cesium lead bromide nanocrystals for improved light-emitting performance, Nanoscale 10 (2018) 4173–4178, <https://doi.org/10.1039/c7nr09126e>.
- [52] H. Wu, Y. Zhang, X. Zhang, M. Lu, C. Sun, T. Zhang, W.W. Yu, Enhanced stability and performance in perovskite nanocrystal light-emitting devices using a ZnMgO interfacial layer, Adv. Opt. Mater. 5 (2017) 1–8, <https://doi.org/10.1002/adom.201700377>.
- [53] J. Kim, S. Cho, F. Dinic, J. Choi, C. Choi, S.M. Jeong, J.S. Lee, O. Voznyy, M.J. Ko, Y. Kim, Hydrophobic stabilizer-anchored fully inorganic perovskite quantum dots enhance moisture resistance and photovoltaic performance, Nano Energy 75 (2020) 104985, <https://doi.org/10.1016/j.nanoen.2020.104985>.
- [54] A. Swarnkar, A.R. Marshall, E.M. Sanehira, B.D. Chernomordik, D.T. Moore, J. A. Christians, T. Chakrabarti, J.M. Luther, Quantum dot-induced phase stabilization of $\$alpha_{\$}-\text{CsPbI}_{3-\delta}$ perovskite for high-efficiency photovoltaics, Science 354 (80) (2016) 92–95. <http://science.sciencemag.org/content/354/6308/92.abstract>.
- [55] M. Yu, D. Zhang, Y. Xu, J. Lin, C. Yu, Y. Fang, Z. Liu, Z. Guo, C. Tang, Y. Huang, Surface ligand engineering of CsPbBr_3 perovskite nanowires for high-performance photodetectors, J. Colloid Interface Sci. 608 (2022) 2367–2376, <https://doi.org/10.1016/j.jcis.2021.10.141>.
- [56] J. Chen, D. Jia, J. Qiu, R. Zhuang, Y. Hu, X. Zhang, Multidentate passivation crosslinking perovskite quantum dots for efficient solar cells, Nano Energy 96 (2022), <https://doi.org/10.1016/j.nanoen.2022.107140>.
- [57] H. Fang, W. Deng, X. Zhang, X. Xu, M. Zhang, J. Jie, X. Zhang, Few-layer formamidinium lead bromide nanoplatelets for ultrapure-green and high-efficiency light-emitting diodes, Nano Res. 12 (2019) 171–176, <https://doi.org/10.1007/s12274-018-2197-3>.
- [58] L. Protesescu, S. Yakunin, M.I. Bodnarchuk, F. Bertolotti, N. Masciocchi, A. Guagliardi, M.V. Kovalenko, Monodisperse formamidinium lead bromide nanocrystals with bright and stable green photoluminescence, J. Am. Chem. Soc. 138 (2016) 14202–14205, <https://doi.org/10.1021/jacs.6b08900>.
- [59] K. Zheng, Q. Zhu, M. Abdellah, M.E. Messing, W. Zhang, A. Generalov, Y. Niu, L. Ribaud, S.E. Canton, T. Pullerits, Exciton binding energy and the nature of emissive states in organometal halide perovskites, Phys. Chem. Lett. 124 (2015) 1–24. <https://pubs.acs.org/doi/abs/10.1021/acs.jpclett.5b01252>.
- [60] H. Huang, F. Zhao, L. Liu, P. Zhang, X.G. Wu, L. Shi, B. Zou, Q. Pei, H. Zhong, Emulsion synthesis of size-tunable $\text{CH}_3\text{NH}_3\text{PbBr}_3$ quantum dots: an alternative route toward efficient light-emitting diodes, ACS Appl. Mater. Interfaces 7 (2015) 28128–28133, <https://doi.org/10.1021/acsami.5b10373>.
- [61] J.D. McGettrick, K. Hooper, A. Pockett, J. Baker, J. Troughton, M. Carnie, T. Watson, Sources of $\text{Pb}(0)$ artefacts during XPS analysis of lead halide perovskites, Mater. Lett. 251 (2019) 98–101, <https://doi.org/10.1016/j.mattlet.2019.04.081>.
- [62] M. Liu, G. Zhong, Y. Yin, J. Miao, K. Li, C. Wang, X. Xu, C. Shen, H. Meng, Aluminum-doped cesium lead bromide perovskite nanocrystals with stable blue photoluminescence used for display backlight, Adv. Sci. 4 (2017) 1–8, <https://doi.org/10.1002/advs.201700335>.
- [63] F. Zhang, H. Zhong, C. Chen, X.G. Wu, X. Hu, H. Huang, J. Han, B. Zou, Y. Dong, Brightly luminescent and color-tunable colloidal $\text{CH}_3\text{NH}_3\text{PbX}_3$ (X = Br, I, Cl) quantum dots: potential alternatives for display technology, ACS Nano 9 (2015) 4533–4542, <https://doi.org/10.1021/acs.nano.5b01154>.
- [64] M. Goto, N. Oshita, K. Yoshida, T. Iizuka, Y. Morikawa, H. Shimizu, R. Kobayashi, T. Chiba, S. Asakura, A. Masuhara, Blue-emitting perovskite nanocrystals with enhanced optical properties through using NaBH_4 , Appl. Phys. Express 17 (2024) 0–5, <https://doi.org/10.35848/1882-0786/ad52e6>.
- [65] F.C. Hanusch, E. Wiesenmayer, E. Mankel, A. Binek, P. Angloher, C. Fraunhofer, N. Giesbrecht, J.M. Feckl, W. Jaegermann, D. Johrendt, T. Bein, P. Docampo, Efficient planar heterojunction perovskite solar cells based on formamidinium lead bromide, J. Phys. Chem. Lett. 5 (2014) 2791–2795, <https://doi.org/10.1021/jz501237m>.
- [66] F. Zhang, B. Yang, K. Zheng, S. Yang, Y. Li, W. Deng, R. He, Formamidinium Lead Bromide (FAPbBr_3) perovskite microcrystals for sensitive and fast photodetectors, Nano-Micro Lett. 10 (2018) 1–8, <https://doi.org/10.1007/s40820-018-0196-2>.
- [67] M.I. Saidaminov, A.L. Abdelhady, G. Maculan, O.M. Bakr, Retrograde solubility of formamidinium and methylammonium lead halide perovskites enabling rapid single crystal growth, Chem. Commun. 51 (2015) 17658–17661, <https://doi.org/10.1039/c5cc06916e>.
- [68] F. Ambroz, W. Xu, S. Gadipelli, D.J.L. Brett, C.T. Lin, C. Contini, M.A. McLachlan, J.R. Durrant, I.P. Parkin, T.J. Macdonald, Room temperature synthesis of phosphine-capped lead bromide perovskite nanocrystals without coordinating solvents, Part. Part. Syst. Charact. 37 (2020), <https://doi.org/10.1002/ppsc.201900391>.
- [69] Z.A. Al-ahmed, N.A. Alenazi, A.R.Z. Almotairy, S. Sallam, H. Alharbi, S.F. Ibarham, N.D. Alkhathami, N.M. El-metwaly, N.A. Alenazi, A.R.Z. Almotairy, S. Sallam, H. Alharbi, S.F. Ibarham, N.D. Alkhathami, N.M. El-metwaly, Remarkable recycling processes of conjugated polymers with titanium dioxide quantum dots as photocatalysts for photodegradation of hazardous industrial wastewater, (2024) 0–36.
- [70] Y. Huang, W. Luan, M. Liu, L. Turianska, DDAB-assisted synthesis of iodine-rich CsPbI_3 perovskite nanocrystals with improved stability in multiple environments, J. Mater. Chem. C 8 (2020) 2381–2387, <https://doi.org/10.1039/c9tc06566k>.
- [71] Y. Chang, Y.J. Yoon, G. Li, E. Xu, S. Yu, C.H. Lu, Z. Wang, Y. He, C.H. Lin, B. K. Wagner, V.V. Tsukruk, Z. Kang, N. Thadhani, Y. Jiang, Z. Lin, All-Inorganic perovskite nanocrystals with a stellar set of stabilities and their use in white light-emitting diodes, ACS Appl. Mater. Interfaces 10 (2018) 37267–37276, <https://doi.org/10.1021/acsami.8b13553>.
- [72] Y. Ai, X. Liu, B. Yang, Q. Li, S. Liu, Lead sulfide quantum dot assembly with biocompatible mechanical property and tunable hydrophilicity, Mater. Sci. Semicond. Process. 140 (2022), <https://doi.org/10.1016/j.mss.2021.106374>.
- [73] J. Chen, J. Lv, X. Liu, J. Lin, X. Chen, A study on theoretical models for investigating time-resolved photoluminescence in halide perovskites, Phys. Chem. Chem. Phys. 25 (11) (2023) 7574–7588, <https://doi.org/10.1039/D2CP05723A>.
- [74] F.X. Xie, D. Zhang, H. Su, X. Ren, K.S. Wong, M. Grätzel, W.C.H. Choy, D. Shi, et al., Low trap-state density and long carrier diffusion in organolead trihalide perovskite single crystals //Science. –2015. –V. 347. –Nº. 6221. –P. 519–522, ACS Nano 9 (2015) 639–646, <https://pubs.acs.org/doi/10.1021/nm505978r>.
- [75] A.S.S. Bilal, M.M. Bilal, M.F. Zia, S. Feroz, M.N. Ullah, M.A. Khan, N. Bano, I. Hussain, R. Fatima, Dual interfacial modification of hematite electron transport layer for efficient and stable perovskite solar cells, Results Eng. 25 (2025) 103954, <https://doi.org/10.1016/j.rineng.2025.103954>.
- [76] R. Estrada, J. Liman, B. Harsono, I. Karnadi, Characterization of small molecule-based organic photodetectors for non-fullerene bulk heterojunction with strong response in the visible light region, Results Eng. 25 (2025) 104009, <https://doi.org/10.1016/j.rineng.2025.104009>.